Controllable photon-phonon conversion via the topologically protected edge channel in an optomechanical lattice

Ji Cao,[1] Wen-Xue Cui,[2] X. X. Yi,[1,*] and Hong-Fu Wang[1,2,†]

[1]*Center for Quantum Sciences and School of Physics, Northeast Normal University, Changchun 130024, China*

[2]*Department of Physics, College of Science, Yanbian University, Yanji, Jilin 133002, China*

(Received 31 October 2020; accepted 19 January 2021; published 5 February 2021)

We propose a scheme to achieve the periodically modulated Su-Schrieffer-Heeger model based on a one-dimensional optomechanical lattice. We show the energy-eigenvalue spectrum and the winding number to demonstrate two topologically distinct phases of the Su-Schrieffer-Heeger model. Specifically, we realize the photon-phonon conversion process via the topologically protected edge channel with a controllable conversion efficiency. By calculating the fidelities of the photon-phonon conversion, we find that our system is more robust against the on-site defect potential throughout the overall lattice sites than the edge lattice sites. Interestingly, the large defect added into the edge sites can induce additional quantum channels to achieve the photon-photon transfer and the phonon-phonon transfer. Our scheme opens an alternative avenue to investigate the topological phases and the quantum state transfer in optomechanical lattice systems.

DOI: 10.1103/PhysRevA.103.023504

I. INTRODUCTION

A topological insulator [1–4] is a new form of matter that behaves as an insulator in its interior while behaving as a metal on its boundary and has been one of the most intriguing research fields in condensed-matter physics. The significant difference between traditional insulators and topological insulators is the presence of the gapless edge states in the nontrivial phase region accompanied with a nontrivially topological index. The Su-Schrieffer-Heeger (SSH) model, as one of the simplest one-dimensional (1D) tight-binding topological models, is characterized by the robust edge state immune to disorders and perturbations. Despite its simplicity, it has attracted extensive studies in the past decades since it exhibits rich physical phenomena, such as the topological phase transition [5–9], edge state and topological invariants [10–16], and non-Hermitian bulk-boundary correspondence [17–24]. Furthermore, it is found that the SSH model can be mapped by various systems, including off-diagonal bichromatic optical lattice [25], graphene ribbon [26], a *p*-orbit optical ladder system [27], circuit QED systems [28–30], etc.

In recent years, tremendous progress has been made in optomechanical systems [31–35], in which optical cavity fields are coupled to mechanical resonators through the effects of radiation pressure or optical gradient forces. The optomechanical systems have been proposed and become excellent platforms to investigate diverse quantum physics, such as quantum information processing [36,37], photon blockade [38–40], photon-phonon entanglement [41], quantum state transfer [42–44], etc. Furthermore, another exciting development is that the optomechanical lattice system can be used to map the topological tight-binding models and study the conversion between photons and phonons. In an optomechanical resonator, the optical and mechanical excitations can be coherently converted, which induces a transparency window for a weak probe laser beam [45]. The single photon-phonon converter has been realized by combining the single-bit operation with the cross-Kerr nonlinear effect in quadratically coupled optomechanical systems [46]. The observation of parametric frequency conversion between two microwave modes mediated by the motion of a mechanical resonator has been reported in Ref. [47]. Therefore, optomechanical systems have become excellent candidates to simulate quantum many-body systems and manipulate the photon and the phonon.

In this paper, inspired by the matter mentioned above, we propose a scheme to induce the topological SSH phase based on an optomechanical lattice, in which the topologically distinct phases can be characterized by the relation between the winding and the origin in the momentum space. Moreover, we investigate the photon-phonon conversion process via the topologically protected edge state with a special distribution under an appropriate parameter regime. Especially, the initial photon state can also be converted into the photon state with an arbitrary conversion efficiency via modulating the varying rate. When the first optical cavity is excited, we find that the photon appears in the first optical cavity and the phonon appears in the last mechanical resonator simultaneously with a certain proportion after a certain time evolution. By numerically calculating the conversion fidelities, we find that the system still possesses a high conversion efficiency against the on-site defect potential throughout the overall lattice sites. However, the photon can be localized in the first site all the time for a nonadiabatic evolution process when the varying rate is large enough. Furthermore, we find that the photon-photon transfer and the phonon-phonon transfer can be achieved via the additional quantum channels

*yixx@nenu.edu.cn
†hfwang@ybu.edu.cn

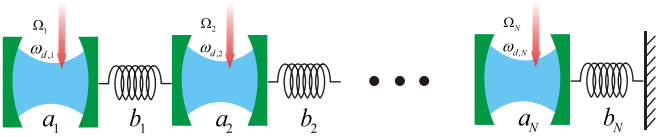

FIG. 1. Schematic of the 1D optomechanical lattice, which is composed by N unit cells. Each unit cell contains an optical cavity, a_n, and a mechanical resonator, b_n. The coupling between the mechanical resonator b_n and two adjacent cavity fields is g_n.

induced by the large defect added into the edge sites. Our scheme reveals a great potential application of topological matter for photon-phonon conversion in quantum information processing.

The rest of the paper is organized as follows. In Sec. II, we propose a method to realize the SSH model based on an optomechanical lattice and demonstrate the topology of the system. In Sec. III, we achieve the photon-phonon conversion via the topological edge channel. In Sec. IV, we discuss the effect of the on-site defect on photon-phonon conversion. Moreover, we show that the large defect added into the edge sites induces the additional topological channels to achieve the photon-photon transfer and phonon-phonon transfer. Finally, a conclusion is given in Sec. V.

II. MODEL AND HAMILTONIAN

We consider a 1D optomechanical lattice composed of N optical cavities and N mechanical resonators, in which each cavity field is driven by an external laser with frequency $\omega_{d,n}$ and amplitude Ω_n, as depicted in Fig. 1. The Hamiltonian of the system is described by ($\hbar = 1$)

$$H = \sum_n \omega_{a,n} a_n^\dagger a_n + \omega_{b,n} b_n^\dagger b_n + \Omega_n e^{-i\omega_{d,n}t} a_n^\dagger + \Omega_n^* e^{i\omega_{d,n}t} a_n - g_n (a_n^\dagger a_n - a_{n+1}^\dagger a_{n+1})(b_n^\dagger + b_n), \quad (1)$$

where $a_n^\dagger (b_n^\dagger)$ and $a_n (b_n)$ are the creation and annihilation operators of the optical cavity field (mechanical resonator) with frequency $\omega_{a,n}(\omega_{b,n})$, respectively. The first two terms represent the energy of the cavity fields and the mechanical resonators, the third and fourth terms correspond to the interactions between external lasers and the cavity fields, and the last term describes the couplings between cavity fields and the mechanical resonators. In the rotating frame with respect to the external laser frequency $\omega_{d,n}$, the Hamiltonian of the system becomes

$$H_1 = \sum_n \Delta_{a,n} a_n^\dagger a_n + \omega_{b,n} b_n^\dagger b_n + \Omega_n a_n^\dagger + \Omega_n^* a_n - g_n (a_n^\dagger a_n - a_{n+1}^\dagger a_{n+1})(b_n^\dagger + b_n), \quad (2)$$

where $\Delta_{a,n} = \omega_{a,n} - \omega_{d,n}$ is the frequency detuning of the cavity fields with respect to the external lasers. Under the condition of strong laser driving, we perform the standard linearization process by rewriting the operators as $a_n = \langle a_n \rangle + \delta a_n = \alpha_n + \delta a_n$ and $b_n = \langle b_n \rangle + \delta b_n = \beta_n + \delta b_n$. After dropping the notation "δ" for all the fluctuation operators δa_n (δb_n), the linearized Hamiltonian can be given by

$$H_1 = \sum_n \Delta'_{a,n} a_n^\dagger a_n + \omega_{b,n} b_n^\dagger b_n - g_n \alpha_n^* a_n b_n^\dagger - g_n \alpha_n^* a_n b_n - g_n \alpha_n a_n^\dagger b_n^\dagger - g_n \alpha_n a_n^\dagger b_n + g_n \alpha_{n+1}^* a_{n+1} b_n^\dagger + g_n \alpha_{n+1}^* a_{n+1} b_n + g_n \alpha_{n+1} a_{n+1}^\dagger b_n^\dagger + g_n \alpha_{n+1} a_{n+1}^\dagger b_n, \quad (3)$$

where $\Delta'_{a,1} = \Delta_{a,1} - g_1(\beta_1^* + \beta_1)$ and $\Delta'_{a,n\in[2,N]} = \Delta_{a,n} + g_{n-1}(\beta_{n-1}^* + \beta_{n-1}) - g_n(\beta_n^* + \beta_n)$ are the effective cavity field detunings originating from the optomechanical coupling. Then, by performing another rotating transformation with respect to $\Delta'_{a,n} a_n^\dagger a_n$ and $\omega_{b,n} b_n^\dagger b_n$, we obtain

$$\begin{aligned} H_1' = \sum_n \big[& - g_n \alpha_n^* e^{-i(\Delta'_{a,n} - \omega_{b,n})t} a_n b_n^\dagger \\ & - g_n \alpha_n^* e^{-i(\Delta'_{a,n} + \omega_{b,n})t} a_n b_n \\ & - g_n \alpha_n e^{i(\Delta'_{a,n} + \omega_{b,n})t} a_n^\dagger b_n^\dagger \\ & - g_n \alpha_n e^{i(\Delta'_{a,n} - \omega_{b,n})t} a_n^\dagger b_n \\ & + g_n \alpha_{n+1}^* e^{-i(\Delta'_{a,n+1} - \omega_{b,n})t} a_{n+1} b_n^\dagger \\ & + g_n \alpha_{n+1}^* e^{-i(\Delta'_{a,n+1} + \omega_{b,n})t} a_{n+1} b_n \\ & + g_n \alpha_{n+1} e^{i(\Delta'_{a,n+1} + \omega_{b,n})t} a_{n+1}^\dagger b_n^\dagger \\ & + g_n \alpha_{n+1} e^{i(\Delta'_{a,n+1} - \omega_{b,n})t} a_{n+1}^\dagger b_n \big]. \end{aligned} \quad (4)$$

Under the red-detuning condition, the counterrotating wave terms can be effectively removed, and the final effective Hamiltonian can be written as

$$H_{\text{eff}} = \sum_n (G_n a_n^\dagger b_n + G_{n+1} a_{n+1}^\dagger b_n) + \text{H.c.}, \quad (5)$$

where $G_n = -g_n \alpha_n$ and $G_{n+1} = g_n \alpha_{n+1}$ are the effective optomechanical couplings. We further modulate the coupling strengths as $G_n = g_0(1 - \cos\theta)$ and $G_{n+1} = g_0(1 + \cos\theta)$, where θ is the modulated parameter in the range of $\theta \in [0, 2\pi]$, and $g_0 = 1$ is the basic effective optomechanical coupling as the energy unit. Note that we can achieve the periodic modulation of system by changing the frequency of the driving field in the way of periodic control [33,48,49]. The optomechanical system can be regarded as a periodically modulated SSH model possessing only the nearest-neighboring couplings; thus the Hamiltonian can be rewritten as

$$H_{\text{SSH}} = \sum_n [(1 - \cos\theta) a_n^\dagger b_n + (1 + \cos\theta) a_{n+1}^\dagger b_n] + \text{H.c.} \quad (6)$$

It is well known that the SSH model holds two distinct phases which can be distinguished by the presence or absence of twofold-degenerate zero-mode edge states. Under the open boundary condition, we plot the energy-eigenvalue spectrum of the system with the lattice size of $N = 5$, in which the phase in the parameter regimes $\theta \in [0, \pi/2] \cup [3\pi/2, 2\pi]$ characterized by the presence of zero-mode edge states is topologically different from the phase in the regime $\theta \in [\pi/2, 3\pi/2]$, as shown in Fig. 2(a). After the Fourier

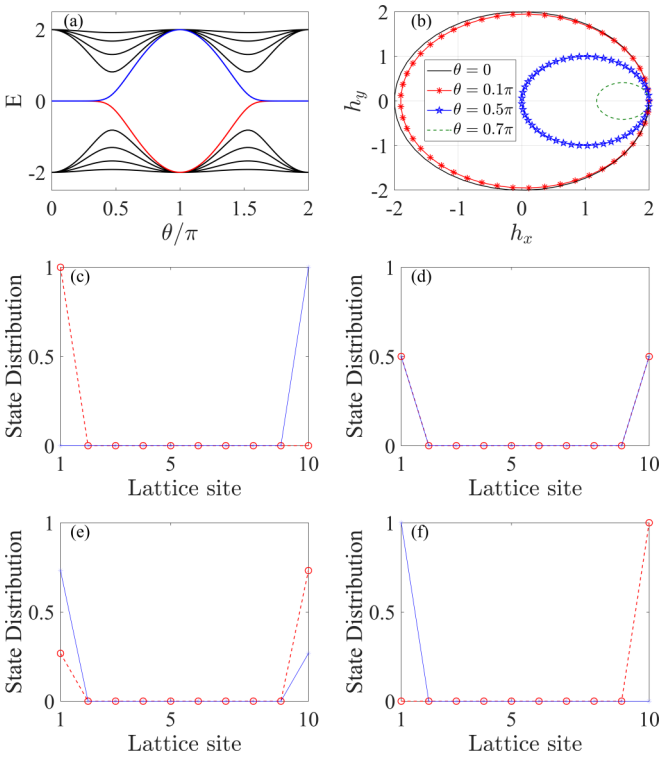

FIG. 2. (a) The energy spectrum of the system. The red line and the blue line represent the Nth and $(N+1)$th eigenvalue versus the periodic parameter θ, respectively. (b) Winding numbers for different parameters θ, including black solid line with $\theta = 0$, red asterisk with $\theta = 0.1\pi$, blue pentagram with $\theta = 0.5\pi$, and green dotted line with $\theta = 0.7\pi$. (c)–(f) The state distributions of the zero-energy modes are defined as $||\psi_n\rangle|^2$, where $|\psi_n\rangle$ is the nth eigenstate of the system. (c) $\theta = 0.001\pi$. (d) $\theta = 0.02\pi$. (e) $\theta = 0.007\pi$. (f) $\theta = 0.002\pi$. The lattice size of the system is $N = 5$.

transformation $\rho_n = \frac{1}{\sqrt{N}} \sum_k e^{ikn} \rho_k$ $(\rho = a, b)$, the Hamiltonian in the momentum space can be expressed as

$$H_{\mathrm{SSH}} = \sum_k \psi_k^\dagger h(k) \psi_k, \tag{7}$$

where $\psi_k^\dagger = (a_k^\dagger, b_k^\dagger)$ and $h(k) = h_x \sigma_x + h_y \sigma_y$ with the Pauli matrix σ acting on the vector ψ_k, $h_x = (1 - \cos\theta) + (1 + \cos\theta)\cos k$, and $h_y = (1 + \cos\theta)\sin k$. The topological properties of the distinct phases can be characterized by the winding angle of $h(k)$ as k varies across the Brillouin zone, i.e., the geometrical meaning of the Zak phase. In Fig. 2(b), we plot the winding numbers to demonstrate the topological properties of the system with four different parameter regimes. The origin is encircled in the winding corresponding to the topologically nontrivial phase, the winding is outside the origin corresponding to the trivial phase, and the winding passes the origin corresponding to the gap closing point. The different winding numbers can characterize the topologically distinct phases in the standard SSH model. According to the bulk-edge correspondence, when the above optomechanical lattice is in a topologically nontrivial phase, the winding number remains unchanged and the topological edge state exhibits a special distribution in its boundary. Since the topologically protected edge states are insensitive to the local defects and disorders,

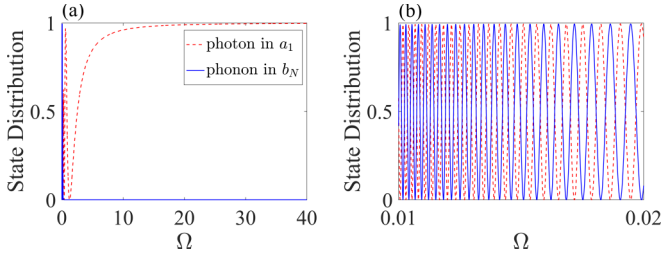

FIG. 3. (a) The photon distribution in the first cavity and the phonon distribution in the last mechanical resonator for the evolved final state versus the varying rate Ω. (b) The detailed patterns of the photon distribution and phonon distribution in the two end sites. The evolution time is $t = 2\pi/\Omega$. The lattice size of the system is $N = 5$.

the topological invariants in our model will endow the edge states to be topologically protected against the disorders and defects. Therefore, such edge states can be employed as the topologically protected quantum channel to realize the robust photon-phonon conversion. To further clarify the topologically distinct phases, we plot the state distributions of the degenerate zero-energy modes in Figs. 2(c)–2(f). Generally speaking, the degenerate zero-mode edge states are simultaneously localized in the two ends of the system with the same distributions in most regions of $\theta \in [0, \pi/2] \cup [3\pi/2, 2\pi]$, as shown in Fig. 2(d). Intriguingly, the state distributions of the two degenerate zero-energy modes can be an arbitrary proportion in the two ends of the system by modulating the parameter θ near 0, as shown in Figs. 2(c)–2(f).

III. PHOTON-PHONON CONVERSION IN THE PERIODICALLY DRIVEN OPTOMECHANICAL LATTICE

In this section, we focus on studying the dynamic process of the system. We rewrite the periodic parameter θ in Eq. (6) as $\theta(t) = \Omega t$, with Ω being the varying rate and t being the time. The corresponding time-dependent Hamiltonian can be written as

$$H_{\mathrm{SSH}}(t) = \sum_n [1 - \cos(\Omega t)] a_n^\dagger b_n + [1 + \cos(\Omega t)] a_{n+1}^\dagger b_n + \mathrm{H.c.} \tag{8}$$

The time evolution of the system is governed by the Schrödinger equation

$$i \frac{d}{dt} |\psi\rangle = H_{\mathrm{SSH}}(t) |\psi\rangle. \tag{9}$$

Suppose that the initial state is $|\psi\rangle_{\mathrm{initial}} = |1\rangle_{a_1} \otimes |0\rangle_{b_1} \otimes |0\rangle_{a_2} \otimes |0\rangle_{b_2} \ldots |0\rangle_{a_N} \otimes |0\rangle_{b_N} = |1, 0, 0, \ldots, 0, 0\rangle$, where the first cavity is excited and the overall dynamic of the system shows a fast-oscillation behavior. As shown in Fig. 3(a), the red dotted line and the blue solid line represent the distributions of the photon and the phonon versus the varying rate Ω, respectively. When Ω is large enough, the photon distribution in a_1 gradually approaches 1 and the phonon distribution in b_N is nearly 0. Moreover, we plot the detailed patterns of the photon distribution in a_1 and the phonon distribution in b_N corresponding to $\Omega \in [0.01, 0.02]$, as shown in Fig. 3(b). We find that the distributions of photons and phonons exhibit a regular periodic pattern. If we choose the varying rate Ω

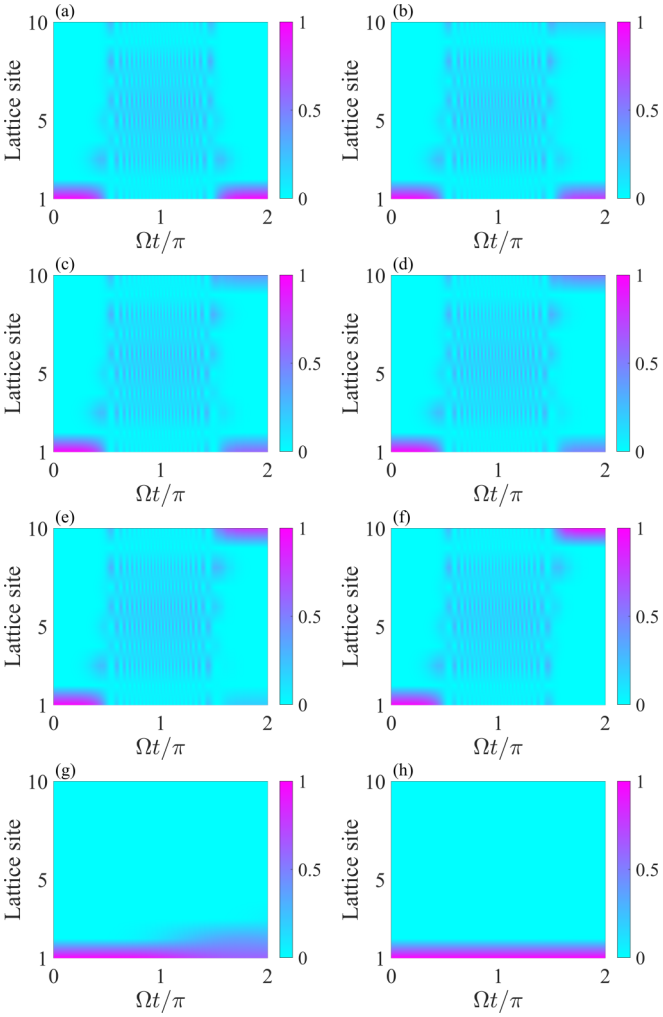

FIG. 4. (a)–(f) The different conversion efficiencies between photons and phonons for various varying rates Ω. (a) 100% :0% with $\Omega = 0.019\,049$. (b) 80% :20% with $\Omega = 0.019\,172$. (c) 60% : 40% with $\Omega = 0.019\,231$. (d) 50% :50% with $\Omega = 0.019\,259$. (e) 20% :80% with $\Omega = 0.019\,347$. (f) 0% :100% with $\Omega = 0.019\,473$. (g) and (h) The photon-phonon conversion with the larger varying rate. (g) $\Omega = 3$. (h) $\Omega = 30$.

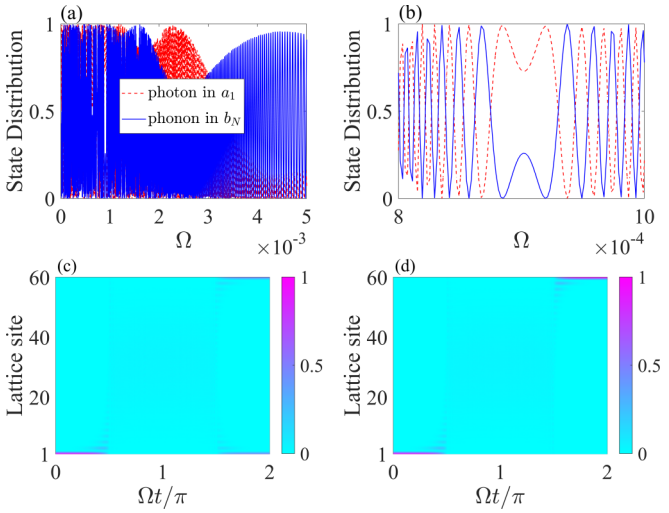

FIG. 5. (a) The photon distribution in a_1 and the phonon distribution in b_n for the evolved final state versus the varying rate Ω. (b) The detailed patterns of the photon distribution and the phonon distribution in the two edge sites. The evolution time is $t = 2\pi/\Omega$. (c) The efficiencies of photon-phonon conversion are 50% :50% for $\Omega = 0.000\,833\,189$. (d) The efficiencies of photon-phonon conversion are 0% :100% for $\Omega = 0.000\,835\,3$. The lattice size of the system is $N = 30$.

appropriately, the photon distribution in a_1 can change from 1 to 0 while the phonon distribution in b_N can change from 0 to 1 simultaneously.

Here, we investigate the photon-phonon conversion process in an appropriate range of the varying rate, such as $\Omega \in [0.019\,049, 0.019\,473]$, and the final state distributions after a certain time evolution are shown in Figs. 4(a)–4(f). For $\Omega = 0.019\,049$, we find that the photon distribution is 100% in the first cavity and no phonon appears in the last mechanical resonator, as shown in Fig. 4(a). One can see from Fig. 4(b) that the photon distribution in a_1 decreases to 80% and the phonons occur in b_N with the proportion of 20% when $\Omega = 0.019\,172$. Similarly, we also exhibit the other different ratios between photon distribution and phonon distribution by choosing the appropriate varying rate Ω, including 60% :40% [Fig. 4(c)], 50% :50% [Fig. 4(d)], 20% :80% [Fig. 4(e)], and 0% :100% [Fig. 4(f)]. It is indicated that we can achieve the conversion process from photon to phonon with an arbitrary proportion by continuously modulating the varying rate Ω. In addition, we consider two cases where the varying rate Ω is larger, as shown in Figs. 4(g) and 4(h). One can see that the evolved final state is only localized in the first two sites when $\Omega = 3$, as shown in Fig. 4(g). In Fig. 4(h), we find that the evolved final state is completely composed of the photon in the first optical cavity with $\Omega = 30$ due to the nonadiabatic evolution. Therefore, the realization of photon-phonon conversion needs to satisfy a condition that the varying rate Ω should be chosen in an appropriate region near 0.

Furthermore, we study the photon-phonon conversion for a large lattice size $N = 30$. In Fig. 5(a), we show the distributions of the photons and phonons versus the varying rate Ω. And we plot the detailed patterns of the photon distribution in a_1 and the phonon distribution in b_N within a minor range of $\Omega \in [0.0008, 0.001]$, which still exhibits a regular pattern, as shown in Fig. 5(b). We take two different conversion efficiencies between photons and phonons as the examples, the photon-phonon conversion can be realized by appropriately choosing the varying rates Ω, as displayed in Figs. 5(c) and 5(d). However, the very tiny parameter is not easy to manipulate compared with the small lattice size in realistic experiments, and the adiabatic evolution condition cannot be well satisfied.

In practice, the system parameters cannot be perfectly tuned to exact values due to the intrinsic fluctuations in device fabrication. The present scheme can be naturally immune against the local disorder and perturbation because the photon-phonon conversion is assisted by the topologically protected zero-energy channel. It is necessary to analyze the influence of imperfect factors added into our scheme, that is, adding a disorder item $W\delta$ into the effective hopping strengths

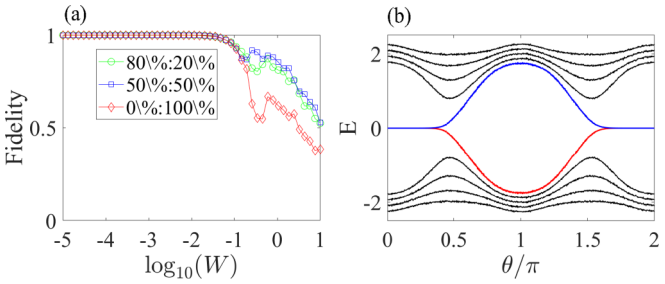

FIG. 6. (a) The fidelity versus the disorder strength with three different conversion efficiencies between photons and phonons. (b) The energy spectra of the SSH model vs θ for the disorder strength $W = 0.6g_0$.

G_n and G_{n+1}, with W being the disorder strength and δ being the random number in the range of $[-0.5, 0.5]$. Taking three different conversion efficiencies as the examples, we numerically calculate the fidelity as a function of the disorder strength W, as shown in Fig. 6(a). It can be seen that the fidelity of our scheme can exceed 90% when $W < 0.1$, which is also a hallmark of the topologically assisted photon-phonon conversion. Moreover, the energy spectrum with the disorder strength $W = 0.6g_0$ is shown in Fig. 6(b), which verifies that the zero-energy edge state is topologically protected. Comparing with the previous works [45–47] with respect to the photon-phonon conversion, we use the optomechanical array to achieve the periodically modulated SSH model with topologically nontrivial phase. Since the zero-energy edge states hold the special distributions, we can achieve the controlled photon-phonon conversion based on the topologically protected zero-energy edge channel, and our scheme can be achieved with a high fidelity against the mild disorder.

IV. EFFECT OF ON-SITE DEFECT ON QUANTUM STATE TRANSFER

Next, we analyze and discuss the effect of on-site defects on the current system, where the on-site potential strength is assumed as V. As depicted in Fig. 7(a), we first plot the energy-eigenvalue spectrum when the defect is added into the first cavity with $V = 0.3$, and the original two degenerate zero-energy edge states become nondegenerate. Meanwhile, we plot the fidelity of the photon-phonon conversion versus the on-site defect V with ignoring the phase, and we find that the conversion fidelity can exceed 50% when the defect strength $\log_{10}(V) < -1$, as shown in Fig. 7(b). Moreover, we also investigate the effect of adding the defect into the overall lattice sites on the photon-phonon conversion. In Fig. 7(c), it can be seen that the energy spectrum only integrally moves up a certain distance with $V = 0.3$, and the degenerate edge states still exist. The corresponding fidelity versus the on-site defects is shown in Fig. 7(d), we find that the fidelity beyond 99.9% can be achieved for a certain range of defect strength with $-2 < \log_{10}(V) < 2$ since the photon-phonon conversion based on the edge states is still topologically protected. Our results verify that the photon-phonon conversion is insensitive to adding the defect into the overall lattice sites compared with the edge lattice sites.

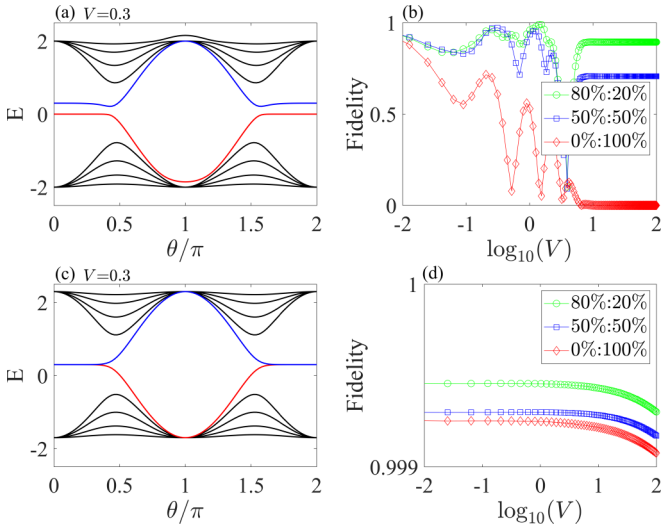

FIG. 7. (a) Energy spectrum of the system when the defect is added into the first site with $V = 0.3$. (b) The fidelity versus the defect potential with three different conversion efficiencies between photons and phonons. (c) Energy spectrum of the system when the defects are added into the overall sites with $V = 0.3$. (d) The fidelity versus the defect potential with three different conversion efficiencies. Other parameter takes $N = 5$.

On the other hand, we find the interesting results when a large defect strength is added into the edge lattice sites with $V = 8$, as shown in Fig. 8. When the large defect is added into the first cavity, the distribution of the gap state versus θ and the lattice site is displayed in Fig. 8(a). Obviously, the phonon state is localized in the second site with $\theta \in (\pi/2, 3\pi/2)$, and it is localized in the last site with $\theta \in (0, \pi/2)$ and $\theta \in (3\pi/2, 2\pi)$. Accordingly, we also simulate the quantum state transfer process when the second mechanical resonator is

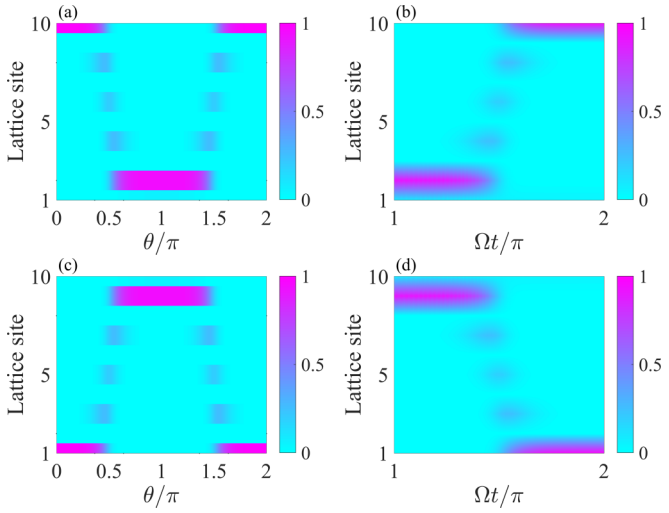

FIG. 8. (a) The distribution of gap state versus θ and the lattice site when the defect is added into the first site with $V = 8$. (b) The phonon-phonon transfer when $\Omega = 0.005$ and $V = 8$. (c) The distribution of the gap state versus θ and the lattice site when the defect is added into the last site with $V = 8$. (d) The photon-photon transfer when $\Omega = 0.005$ and $V = 8$.

excited, and the phonon-phonon transfer can be achieved via a topologically protected channel when $\Omega = 0.005$, as shown in Fig. 8(b). Moreover, when the large defect is added into the last mechanical resonator, the photon state is localized in the penultimate site when $\theta \in (\pi/2, 3\pi/2)$, and it is localized in the first site when $\theta \in (0, \pi/2)$ and $\theta \in (3\pi/2, 2\pi)$, as shown in Fig. 8(c). Similarly, we also successfully achieve the photon-photon transfer via a topological channel with $\Omega = 0.005$ when the penultimate cavity is excited, as shown in Fig. 8(d). These results reveal that the photon-photon transfer and the phonon-phonon transfer can be achieved via the additional quantum channels induced by the large on-site defect added into the edge sites.

Before concluding, we briefly discuss the experimental feasibility of our scheme. Remarkably, the optomechanical system [35] with excellent tunability and scalability has become a mature platform to investigate the properties of various quantum systems. In optomechanical crystals, the frequency of oscillators $\omega_{b,n}$ and the effective optomechanical coupling strength G_n can approach 10^9 Hz order [42], even the effective coupling strength between the cavity and the oscillator can reach the range of THz [50]. Recently, some topological models have been theoretically provided and experimentally realized based on optomechanical systems [43,51]. In the present scheme, we achieve the photon-phonon conversion by using the topologically protected edge states as the quantum channels, and the system parameters can be modulated in a small range by adiabatically controlling the amplitude of the external laser field, which means that one can easily tune the parameters to meet the parameter requirement of our scheme with the state-of-the-art quantum devices [52,53]. Therefore, our scheme is remarkably feasible with the current optomechanics techniques.

V. CONCLUSIONS

In conclusion, we have proposed a scheme to construct the periodically modulated SSH model based on a 1D optomechanical lattice. We have shown the winding number to demonstrate the topologically distinct phases. Especially, the zero-energy edge states can be pumped from the left edge to the right edge by modulating the parameter θ with $\theta \sim 0$. It is indicated that the conversion efficiencies between the photon and the phonon are controllable by appropriately choosing varying rate Ω. However, when Ω is large enough, the final quantum state is always localized in the first cavity because the system undergoes a nonadiabatic evolution process. The photon-phonon conversion is much more robust against the defect throughout the overall system than the edge lattice site. Moreover, the photon-photon transfer and the phonon-phonon transfer can be realized via the additional quantum channels induced by the large defect added into the edge sites. Our scheme provides a controllable platform to engineer the topological phases and opens up a new path to achieve the different quantum state transfers.

ACKNOWLEDGMENT

This work was supported by the National Natural Science Foundation of China under Grants No. 61822114, No. 12074330, No. 11775048, and No. 12047566.

[1] X. L. Qi and S. C. Zhang, Rev. Mod. Phys. **83**, 1057 (2011).
[2] M. Z. Hasan and C. L. Kane, Rev. Mod. Phys. **82**, 3045 (2010).
[3] A. Bansil, H. Lin, and T. Das, Rev. Mod. Phys. **88**, 021004 (2016).
[4] C. K. Chiu, J. C. Y. Teo, A. P. Schnyder, and S. Ryu, Rev. Mod. Phys. **88**, 035005 (2016).
[5] L. Li, Z. Xu, and S. Chen, Phys. Rev. B **89**, 085111 (2014).
[6] L. Li and S. Chen, Phys. Rev. B **92**, 085118 (2015).
[7] Z. Xu, R. Zhang, S. Chen, L. Fu, and Y. Zhang, Phys. Rev. A **101**, 013635 (2020).
[8] E. Fradkin and J. E. Hirsch, Phys. Rev. B **27**, 1680 (1983).
[9] D. J. J. Marchand, G. De Filippis, V. Cataudella, M. Berciu, N. Nagaosa, N. V. Prokof'ev, A. S. Mishchenko, and P. C. E. Stamp, Phys. Rev. Lett. **105**, 266605 (2010).
[10] F. Dangel, M. Wagner, H. Cartarius, J. Main, and G. Wunner, Phys. Rev. A **98**, 013628 (2018).
[11] A. M. Marques and R. G. Dias, Phys. Rev. B **95**, 115443 (2017).
[12] R. Fu, Z. Shuai, J. Liu, X. Sun, and J. C. Hicks, Phys. Rev. B **38**, 6298 (1988).
[13] L. Du, J. H. Wu, M. Artoni, and G. C. La Rocca, Phys. Rev. A **100**, 012112 (2019).
[14] B. Sbierski and C. Karrasch, Phys. Rev. B **98**, 165101 (2018).
[15] C. Yuce and H. Ramezani, Phys. Rev. A **100**, 032102 (2019).
[16] L. Li, C. Yang, and S. Chen, Eur. Phys. J. B **89**, 195 (2016).
[17] X. Z. Zhang and Z. Song, Phys. Rev. A **99**, 012113 (2019).
[18] S. Lieu, Phys. Rev. B **97**, 045106 (2018).
[19] K. Kawabata, K. Shiozaki, and M. Ueda, Phys. Rev. B **98**, 165148 (2018).
[20] L. Jin and Z. Song, Phys. Rev. B **99**, 081103(R) (2019).
[21] T. E. Lee, Phys. Rev. Lett. **116**, 133903 (2016).
[22] F. K. Kunst, E. Edvardsson, J. C. Budich, and E. J. Bergholtz, Phys. Rev. Lett. **121**, 026808 (2018).
[23] S. Yao and Z. Wang, Phys. Rev. Lett. **121**, 086803 (2018).
[24] S. Yao, F. Song, and Z. Wang, Phys. Rev. Lett. **121**, 136802 (2018).
[25] S. Ganeshan, K. Sun, and S. Das Sarma, Phys. Rev. Lett. **110**, 180403 (2013).
[26] P. Delplace, D. Ullmo, and G. Montambaux, Phys. Rev. B **84**, 195452 (2011).
[27] X. Li, E. Zhao, and W. Vincent Liu, Nat. Commun. **4**, 1523 (2013).
[28] L. Qi, Y. Xing, J. Cao, X. X. Jiang, C. S. An, A. D. Zhu, S. Zhang, and H. F. Wang, Sci. China Phys., Mech. Astron. **61**, 080313 (2018).
[29] L. Qi, Y. Xing, G. L. Wang, S. Liu, S. Zhang, and H. F. Wang, Ann. Phys. **532**, 2000067 (2020).
[30] F. Mei, J. B. You, W. Nie, R. Fazio, S. L. Zhu, and L. C. Kwek, Phys. Rev. A **92**, 041805(R) (2015).

[31] S. Gröblacher, K. Hammerer, M. R. Vanner, and M. Aspelmeyer, Nature (London) **460**, 724 (2009).
[32] J. M. Pirkkalainen, S. U. Cho, F. Massel, J. Tuorila, T. T. Heikkilä, P. J. Hakonen, and M. A. Sillanpää, Nat. Commun. **6**, 6981 (2015).
[33] C. H. Bai, D. Y. Wang, S. Zhang, S. Liu, and H. F. Wang, Phys. Rev. A **101**, 053836 (2020).
[34] T. Ramos, V. Sudhir, K. Stannigel, P. Zoller, and T. J. Kippenberg, Phys. Rev. Lett. **110**, 193602 (2013).
[35] M. Aspelmeyer, T. J. Kippenberg, and F. Marquardt, Rev. Mod. Phys. **86**, 1391 (2014).
[36] C. Dlaska, B. Vermersch, and P. Zoller, Quantum Sci. Technol. **2**, 015001 (2017).
[37] F. Mei, G. Chen, L. Tian, S. L. Zhu, and S. Jia, Phys. Rev. A **98**, 012331 (2018).
[38] J. Q. Liao and F. Nori, Phys. Rev. A **88**, 023853 (2013).
[39] D. Y. Wang, C. H. Bai, S. Liu, S. Zhang, and H. F. Wang, Phys. Rev. A **99**, 043818 (2019).
[40] P. Rabl, Phys. Rev. Lett. **107**, 063601 (2011).
[41] U. Akram, W. Munro, K. Nemoto, and G. J. Milburn, Phys. Rev. A **86**, 042306 (2012).
[42] G. D. de Moraes Neto, F. M. Andrade, V. Montenegro, and S. Bose, Phys. Rev. A **93**, 062339 (2016).
[43] L. Qi, G. L. Wang, S. Liu, S. Zhang, and H.-F. Wang, Opt. Lett. **45**, 2018 (2020).
[44] L. Qi, G. L. Wang, S. Liu, S. Zhang, and H. F. Wang, Phys. Rev. A **102**, 022404 (2020).
[45] C. Dong, Z. Shen, C. Zou, and G. Guo, Sci. China Phys., Mech. Astron. **58**, 1 (2015).
[46] T. Y. Chen, W.-Z. Zhang, R. Z. Fang, C. Z. Hang, and L. Zhou, Opt. Express **25**, 10779 (2017).
[47] F. Lecocq, J. B. Clark, R. W. Simmonds, J. Aumentado, and J. D. Teufel, Phys. Rev. Lett. **116**, 043601 (2016).
[48] A. Mari and J. Eisert, Phys. Rev. Lett. **103**, 213603 (2009).
[49] L. Qi, Y. Xing, H. F. Wang, A. D. Zhu, and S. Zhang, Opt. Express **25**, 17948 (2017).
[50] G. Heinrich, M. Ludwig, J. Qian, B. Kubala, and F. Marquardt, Phys. Rev. Lett. **107**, 043603 (2011).
[51] L. L. Wan, X. Y. Lü, J. H. Gao, and Y. Wu, Opt. Express **25**, 17364 (2017).
[52] C. Sanavio, V. Peano, and A. Xuereb, Phys. Rev. B **101**, 085108 (2020).
[53] V. Peano, C. Brendel, M. Schmidt, and F. Marquardt, Phys. Rev. X **5**, 031011 (2015).